RESEARCH ARTICLE

Polypyrrole Modified Granular Activated Carbon Nanocomposite for Treatment of Wastewater Containing Highly Toxic Hexavalent Chromium

Katlego Z. Setshedi,* Lonji Kalombo, Nomvuyo Nomadolo, Lerato Hlekelele, Suprakas Sinha Ray, and Arjun Maity*

This study explored the fabrication of Polypyrrole (PPy) and Granular Activated Carbon (GAC) composites (PPy-GAC) for effective removal of toxic hexavalent chromium (Cr(VI)) from aqueous solutions. Two synthesis methods are employed: (1) electrostatic deposition of PPy onto pre-charged GAC paper and (2) in-situ chemical polymerization of pyrrole monomer with GAC particles. Batch adsorption experiments investigated the impact of various operational parameters on Cr(VI) removal. Compared to pristine GAC (54.64 mg g^{-1}), the PPy-GAC composite exhibited a remarkable 3-fold increase in equilibrium adsorption capacity, reaching 175.44 mg g^{-1}. Pseudo-second-order kinetic model ($R^2 > 0.999$) accurately described the adsorption kinetics, while the Langmuir isotherm model ($R^2 > 0.99$) provided a good fit for the equilibrium data. Maximum adsorption capacity (q_{max}) increased with temperature, reaching 204.08, 243.90, and 270.27 mg g^{-1} at 298, 308, and 318 K, respectively. Furthermore, a fixed-bed column experiment examined the composite's effectiveness in continuous Cr(VI) removal, demonstrating its suitability for practical applications. Notably, the PPy-GAC composite successfully removed Cr(VI) from a real wastewater sample containing 68 μg L^{-1} Cr(VI) obtained from a ferrochrome industry, highlighting its potential for real-world remediation.

K. Z. Setshedi, L. Kalombo, N. Nomadolo, L. Hlekelele, S. S. Ray, A. Maity
DST/CSIR
Centre for Nanostructures and Advanced Materials (CeNAM)
Council for Scientific and Industrial Research (CSIR)
Pretoria 0001, South Africa
E-mail: ksetshedi@csir.co.za; amaity@csir.co.za
S. S. Ray
Department of Chemical Science
University of Johannesburg
Doorfontein, Johannesburg 2028, South Africa
A. Maity
Department of Chemical Engineering
Faculty of Engineering
Built Environment and Information Technology
University of Pretoria
Pretoria 0110, South Africa

1. Introduction

It is well known that water pollution is a major global problem. Only 1% of fresh water is accessible as pure water fit for human consumption; However, population growth, urbanization, and rapid industrialization have increased the pressure on freshwater resources due to unregulated or illegal discharge of contaminated waste or wastewater streams into the environment. A vast number of different complex pollutants, organic compounds, and heavy metals used in modern industrial processes are released into the environment. These can cause both human health problems and environmental disasters. It is further known that heavy metal ions are persistent in the environment since they cannot be degraded. According to the "World's worst pollution problems report" published in 2010 by the Blacksmith Institute, heavy metals are ranked in the top four out of the top six most toxic global pollutant list.[1] Of this list, for example, chromium is ranked the 3rd most toxic pollutant impacting 13–17 million people world-wide. Hexavalent chromium [Cr(VI)] is highly toxic and harmful to living organisms even at low concentrations due to its carcinogenic and mutagenic properties.[2]

This has led the World Health Organization (WHO) to regulate the allowable limits for Cr(VI) in potable and inland surface water as 0.05 mg L^{-1} and 0.1 mg L^{-1}, respectively.[3] To alleviate this, several technologies have been established for wastewater treatment including chemical precipitation, ion exchange, reverse osmosis, electrodialysis, ultrafiltration, nanofiltration, coagulation, flocculation, floatation and adsorption among others;[4] However, each of these conventional technologies has characteristic constraints which often limits their industrial applications in terms of cost, feasibility, efficiency, practicability, reliability, environmental impact, sludge production, operational difficulty, pretreatment requirements and/or the formation of potentially toxic by-products.[5]

Meanwhile, the complexity of these polluting streams requires a radical change in the approach of how the problem needs to be tackled, definitely not by conventional wastewater treatment processes, but by a more robust, compiling and holistic

technology aiming at minimizing the number of steps, thus the overall treatment costs. Adsorption technology has the potential to provide a more holistic approach due to its versatility, economic feasibility, simplicity, and environmental benignity. Different types of adsorbents are used in adsorption process, most commonly activated carbon (AC) for the removal of heavy metals and organic pollutants.[6] Regardless of having several adsorbents utilized for the removal of various pollutants, no single adsorbent has been found to be effective for different types of water pollutants, and as a result limits their application for treatment of complex effluents laden with various pollutants of different chemistries.[7] To address this shortcoming requires materials with sufficient and desirable adsorption properties for simultaneous removal of various pollutants.

Polymer-based adsorbents, including semi-conducting adsorbents such as polypyrrole (PPy), have received much attention owing to their potential application in the removal of heavy metals from aqueous solutions.[8] They offer advantages such as high surface area, porous structure, favorable electrochemical properties, ion exchange capability, facile synthesis, simple operation and regeneration, high stability, and cost effectiveness, which favor their utilization as efficient adsorbents for the removal of water pollutants;[7,8] However, issues related to the poor dispersion of PPy in water, low density, and the tendency to agglomerate in irregular morphology which occasionally reduces the surface area and sorption capacity, often limits its application during high water demand treatment process, where continuous adsorption configurations using fixed-bed columns are favored.

Meanwhile, PPy-based composites composed of different materials, such as carbon nanotubes, chitosan, and bentonite, have recently been employed for the removal of heavy metal ions from aqueous solutions.[9–11] PPy was selected over other similar materials as it holds significant promise as an adsorbent for wastewater treatment due to its remarkable combination of characteristics: Exceptional adsorption capacity, tunable structure, and robust stability. For a single-step removal of inorganic (heavy metals and anions) and organic (from biological or chemical sources) contaminants from wastewater, the proposed research entails the development of a PPy based granular activated carbon (GAC) composite (PPy-GAC), with two distinctive sites and or surface functionalities to allow two types of chemistries (organic and inorganic) to occur on the same particle. These types of composites having biphasic geometry of distinct compositions are called Janus-like particles.[12,13] Therefore, the main objective of the present study entails the development of PPy coated GAC nanocomposites with two distinct surface properties of PPy and GAC using the electrospray coating technique and in situ chemical polymerization technique. The process followed for the synthesis of the composites is given the supporting information document, marked as S1.

The GAC utilized in this study possessed a granular size distribution between 0.6 mm and 1 mm. Particles within this range exhibited excellent settling behavior in the batch reactor, enabling straightforward separation by decantation and, if necessary, gravity filtration. This characteristic significantly simplifies the separation process compared to powder-form adsorbents, which often necessitate the implementation of intricate techniques like centrifugation or membrane filtration.

2. Experimental Section

2.1. Materials

Norit GAC 1240 W was purchased from Yarn-Home & Industry Filters (Johannesburg, South Africa). It was produced by steam activation of coal and suitable for thermal reactivation owing to its exceptional hardness. Other reagents included ferric chloride (FeCl₃) as an oxidant, Tween 20, sodium oleate ($C_{18}H_{33}NaO_2$), polyvinyl alcohol (PVA) (Mw 13—23 kDa, 87–89% hydrolysed) were purchased from Sigma Aldrich, South Africa. Whereas the pyrrole (Py) monomer was supplied by Aily Intl. Chemical Corp. Ltd., South Africa. Moreover, the model contaminants: sodium dichromate ($Na_2Cr_2O_7$), sodium nitrate ($NaNO_3$), sodium phosphate (Na_3PO_4), sodium sulphate were all purchased from Sigma Aldrich, South Africa. The solvents such as ethanol (EtOH) and acetone were of analytical grade and were used without further purification. De-ionised water was used for making up the aqueous solutions. Sodium hydroxide (NaOH), hydrochloric acid (HCl) and sulphuric acid were used to adjust the pH when necessary.

2.2. Materials Synthesis

The nanocomposite adsorbent comprised of two distinct PPy and GAC sides and their combined corresponding chemical and physical properties were prepared via an electro-spraying assisted coating technique of the microemulsion polymerized PPy (*me*PPy) nanoparticles (NPs) onto one surface side of the opposite polarity pre-charged GAC particles. The preparation steps toward the *me*PPy-GAC steps include i) synthesis of *me*PPy-NPs via the micro-emulsion based chemical oxidative polymerization of the Py monomer using FeCl₃ as an oxidant ii) pre-coating substrate (GAC particles) preparations including particle size selection and charging by sieving and tribo-charging techniques, respectively, and iii) single surface side electro-spraying assisted coating process of *me*PPy onto GAC particles. The flow chart for preparation is depicted in supporting information document marked as S1.

2.2.1. PPy Synthesis (mePPy) Using Microemulsion Polymerization in the Presence of Micelles

The *me*PPy-NPs were synthesized by the oxidative micro-emulsion polymerization system of pyrrole monomer with oxidant FeCl₃ adopted from the previously published method.[14] Accordingly, a micellar templating method was employed, wherein the nano-domains of aggregated surfactants were used as nano-reactors for the polymerisation of pyrrole (Py) monomers to yield the *me*PPy-NPs. Briefly, aqueous solutions (100 mL each) of polyvinyl alcohol (PVA) 2% (w/v) and sodium oleate 0.2% (w/v) were separately prepared. Thereafter, 5 mL of sodium oleate solution was added to 5 mL of PVA solution in a 50 mL beaker, to which 1 mL of ethanol and four drops of surfactant Tween 20 were introduced. Finally, the micellar solution temperature was increased to 60 °C and the reaction was left to stir for 5 min while observed the physical changes as previously reported,[15] followed by a rapid quench to room temperature. When a homogenous micellar solution was obtained, the monomer (Py,

0.4 mL) was added dropwise to the solution while stirring. With continuous stirring, the oxidant (FeCl$_3$, 3 g) was introduced to the solution, and polymerization was initiated and under stirring for 3 h at room temperature. The final product, i.e PPy nanoparticles (*me*PPy-NP), was then collected by centrifuging at 21 000 rpm using a high-speed refrigerated centrifuge and purified by washing with acetone. The washed nanoparticles pellet was snap frozen in liquid nitrogen and freeze dried for 6 h in a Virtis Freeze Dryer. The dried *me*PPy-NPs were then collected for characterization and further electro-spraying coating process onto GAC surface.

With the same molar ratio of oxidant to monomer, a conventional aqueous solution polymerization for the synthesis of PPy was also carried out for comparison. In a typical approach, the oxidant was dissolved in 40 mL of deionized water in a 250 mL conical flask. Then, 0.4 mL of Py was introduced dropwise into the oxidant solution and left to stir for 3 h at room temperature. The reaction was then stopped by adding 10 mL of acetone, and the resulting slurry of PPy was filtered and washed with deionised water to remove unreacted FeCl$_3$ followed by acetone to wash off oligomers. The black PPy precipitate was then dried under vacuum at 80 °C for 6 h.

2.2.2. Adsorbent Synthesis

The GAC particles received from the supplier were first sieved on a vibrator to screen out the preferred range of particle size for better adsorption kinetics while maintaining an acceptable pressure drop in the column. The fraction −18 to +30 Mesh size of the ASTM sieves were preferably considered equivalent to particle size ranging between 1 mm and 0.600 mm.

2.2.3. Electro-Spraying Technique

The synthesis of the mePPy-GAC composites was carried out by the electrostatic deposition of mePPy particles onto one half of the tribocharged GAC surface by an electro-spraying technique. Driven by the advantages of controlled diameter and morphology, minimized agglomeration, improved adhesion to the GAC substrate, and inherent scalability, the electro-spraying technique was implemented to deposit PPy onto the GAC surface. First, the GAC particles were prepared for electro-spraying via the tribocharging method, involving frictional contact between the GAC particles and an electrostatically charged with the opposite polarity. Typically, the friction causes electrons to transfer between surfaces, where the resulting charges on both surfaces contribute electrostatic forces to their mutual interactions.[16,17] Accordingly, the GAC particles were tribo-charged paper (P), Tribo-charging was then carried out by rolling, rubbing, and bouncing the GAC particles on the P surface, inducing and transferring electrostatic charges onto the GAC particles surface.

Meanwhile, in a typical electro-spraying process, the solution of *me*PPy nanosuspension was filled in a 20 mL-plastic syringe-pump with a stainless-steel capillary (26 G-needle) connected to the positive electrode. The spraying time was 30 min and distance between the nozzle and the collector fixed at 8 cm. Accordingly, the nanosuspension was electro-sprayed over 1.5 g of the charged GAC particles surface, placed on top of the negative electrode covered with aluminum foil that was electrically grounded,

to produce half-moon-like PPy coated GAC particles by using a high voltage power supply generating ±15 to 20 kV potential difference between the nozzle and the ground aluminum foil. The resulting electro-sprayed nanocomposites were labelled as P-*me*PPy-GAC.

2.2.4. In Situ Chemical Oxidative Polymerization Technique

The (in situ)-PPy-GAC synthesis was carried out via the in situ chemical oxidative polymerization technique of the Py monomer in the presence of GAC particles using FeCl$_3$ as an oxidant. The synthesis process was chosen to maximize the dispersion uniformity of the polymer on the GAC, thus providing strong interactions between the two materials. In a typical process, 1 g of GAC and 0.8 mL of Py were added to a 250 mL conical flask and slowly stirred for 1 h. Next, 80 mL of the FeCl$_3$ (0.04 M) aqueous solution was slowly added dropwise to the suspension, and polymerization was allowed to proceed under constant stirring for 3 h at room temperature. The reaction was then stopped by adding 10 mL of acetone and the resulting (in situ)-PPy-GAC composite slurry was filtered, washed with deionised water and finally dried at 60 °C under vacuum for 8–10 h.

2.3. Characterization

Particle size and particle size distribution, the latter expressed as PDI (polydispersity index), were measured by dynamic laser scattering or photon correlation spectroscopy using a Malvern Zetasizer Nano ZS (Malvern Instruments, Worcestershire, United Kingdom). Each sample was tested in triplicate by suspending a little amount of powder in distilled water or, if the sample was liquid, by measuring it in liquid form. It was analyzed undiluted so as to prevent the de-stabilization of the emulsion. The intensity-weighted mean value was calculated using the average of three independent measurements. A Malvern Zetasizer Nano ZS was used to determine the Zeta potential at 25 °C. BET specific surface area was determined by using a Tristar II 3020 Surface area analyser using N$_2$ adsorption-desorption method (−195.8 °C). Fourier transform infrared (FTIR) analysis was carried out on the FTIR spectrometer (PerkinElmer Spectrum100, USA) using FTIR grade KBr as a reference material, and data was obtained in transmittance mode in the range 4000–400 cm^{-1} with a spectral resolution of 4 cm^{-1}. The surface morphological and structural features were studied using the scanning electron microscope (SEM; JEOL JSM-7500F, Japan), while the high-resolution transmission electron microscope (HRTEM; JEOL, 2100-JEM Japan) operated at a voltage of 200 kV was used to investigate the structural features of the prepared materials.

2.4. Adsorption Experiments

2.4.1. Effect of pH

The influence of solution pH on the adsorption of Cr(VI) onto P-mePPy-GAC was evaluated in a batch adsorption mode, by varying the initial Cr(VI) solution pH with the range 2–8, using either 0.05–0.1 M NaOH or HCl. In a typical experiment, 0.15 g of

P-mePPy-GAC was contacted with 50 mL of 200 mg L^{-1} Cr(VI) solution inside plastic bottles, and agitated at 200 rpm for 24 h in a thermostatic shaker. The samples were filtered and residual Cr(VI) concentration was then measured by the Perkin Elmer Lambda UV–Vis spectrometer at 540 nm using 1,5 diphenylcarbazide reagent. The Cr(VI) removal percentage was determined by using the Equation (1):

$$\% \text{ Removal} = \frac{C_o - C_e}{C_e} \times 100 \tag{1}$$

where C_o and C_e are the initial and the equilibrium concentration (mg/L) of Cr(VI), respectively.

2.4.2. Batch Adsorption Kinetics

Kinetics of adsorption gives a relationship between the adsorbed amounts of Cr(VI) onto the adsorbent and contact time in order to extract essential information about the adsorption mechanisms. The adsorption kinetic experiments were carried out in a 1 L glass beaker used as a batch reactor, and the initial Cr(VI) concentration fixed at 200 mg L^{-1}. To a 1 L aqueous solution of Cr(VI), 1.5 g of the adsorbent was added and the solution was stirred at 200 rpm using an overhead stirrer. At predetermined time intervals, 6 mL of aliquots were withdrawn from the reactor, filtered and analyzed for residual Cr(VI) concentration. The Cr(VI) concentration was analyzed according to UV–Vis (Perkin Elmer Lambda 35) spectrophotometric method at a wavelength of 540 nm with 1,5-diphenylcarbazide reagent. The amounts of Cr(VI) ions adsorbed per unit mass q_t of adsorbent at any time (t) were calculated using Equation (2):

$$q_t = \left(\frac{C_o - C_t}{m} \right) V \tag{2}$$

where C_o and C_t are initial and the time dependent bulk phase concentrations (mg L^{-1}), respectively, while V (L) is the bulk sample volume and m (g) is the mass of the used adsorbent. The kinetic studies performed herein includes the performance evaluation and comparison of the PPy, GAC, (in-situ)-PPy-GAC, and P-mePPy-GAC for Cr(VI) removal.

2.4.3. Adsorption Isotherms

The equilibrium Cr(VI) sorption isotherm data were generated by agitating 0.15 g of the adsorbent with 50 mL solutions of varying Cr(VI) concentrations (100–600 mg L^{-1}) in 100 mL screw-cap plastic bottles using a thermostatic shaker. The samples were agitated at 200 rpm for 24 h. Moreover, the effect of temperature on Cr(VI) sorption equilibrium isotherms was evaluated for varying reaction temperatures from 298, 308, and 318 K. After equilibrium attainment, the samples were filtered and analyzed for residual Cr(VI) concentrations. The amounts of Cr(VI) adsorbed at equilibrium were determined using Equation (3):

$$q_e = \left(\frac{C_o - C_e}{m} \right) V \tag{3}$$

Table 1. Summarize the BET surface areas of GAC, mePPy- NPs and P-mePPy-GAC.

Materials	BET Surface Area [m^2/g]
GAC	870
mePPy-NPs	500
P-mePPy-GAC	137

where q_e is the equilibrium amount of Cr(VI) adsorbed per unit mass (m) of adsorbent (mg/g) and V is the sample volume (L).

2.4.4. Fixed-Bed Column Adsorption Dynamics of the P-mePPy-GAC and GAC

The performance of the adsorbent for Cr(VI) removal in practical industrial wastewater treatment where batch systems are replaced by continuous operations, was evaluated using a fixed-bed adsorption column configurations. Continuous fixed-bed column adsorption studies of Cr(VI) were performed using a 30 cm high lab scale perspex cylindrical tube of 1.6 cm internal diameter as column model. The column was packed with the adsorbent between glass wool and supported by inert glass beads.

Subsequently, the influent Cr(VI) solution of 10 mg L^{-1} was pumped in an upward flow at 3 mL m^{-1}n through the 4 cm high packed bed using a peristaltic pump. The upward flow mode was chosen to ensure complete contact between the influent solution and the packed-bed, while the influent Cr(VI) concentration of 10 mg L^{-1} was chosen as a model to represent the common concentration profile of Cr(VI) in wastewater. Furthermore, a comparative Cr(VI) removal performance study was carried out using unmodified GAC under similar experimental fixed-bed column adsorption experiments.

3. Results and Discussion

3.1. Characterization

The BET surface area of the GAC decreased after treatment with the nanoparticles. A decline in surface area of P-mePPy-GAC nanocomposites to as low as 137 m^2 g^{-1} on average was observed following the electro-spraying of mePPy-NPs onto the surface of GAC particles. This decrease is likely to be a consequence of the coverage of pores on GAC surface by the film of mePPy-NPs, even though their specific surface area was initially about 500 m^2 g^{-1} as in **Table 1**.

The mePPy-NPs had their particle size and PDI ranging between (200 nm–245 nm) and (0.2–0.3), respectively. The microemulsion used as the "soft" template for oxidative polymerization of PPy-NPs had a droplet size averaging 3 nm. The zeta potential of mePPy-NPs was found to be positive 38 mV in accordance with the literature.[18] The GAC particles were first sieved through the ASTM sieves ranging from −18 to +30 Mesh size targeting a particle size ranging between 0.600 and 1 mm. Their zeta potential averaged 15 mV when suspended in deionized water with an isoelectric point between pH 4 and 5. This point-of-zero charge (PZC) was shifted toward neutral pH when the
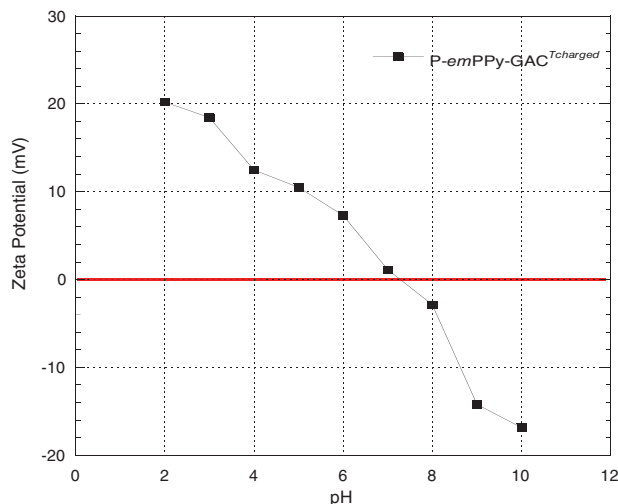
Figure 1. The point-of-zero charge of P-mePPy-GAC composite.

nanocomposite was formed and reached pH 7.2 for P-*me*PPy-GAC nanocomposite as shown by the zero-line intercept with the graph plotted in **Figure 1**.

The FTIR spectrum of P-*me*PPy-GAC in **Figure 2** shows a broad peak at 3222 cm^{-1} which is indicative of both free and hydrogen bonded O-H groups on the GAC surface. The characteristic peaks at 1540 cm^{-1} and 1443 cm^{-1} are related to the C-C and C-N stretching vibration in the PPy ring, respectively. The peaks at 1268 cm^{-1}, 1168 cm^{-1} and 1032 cm^{-1}, may be attributed to C-O-C stretching, while the peaks at 1168 cm^{-1} and 1032 cm^{-1} are consistent with the alcoholic C-O and C-N stretching vibrations in-plane -C-H vibrations.[19] Moreover, 773 cm^{-1} and 691 cm^{-1} are ascribed to the C-H out-of-plane deformational vibration mode of the PPy ring, suggesting a successfully coating of PPy onto the GAC surface.
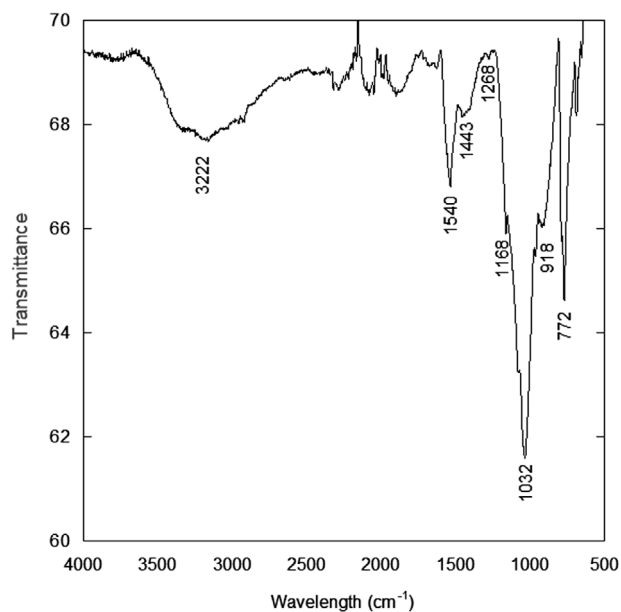

Figure 2. FTIR spectrum of P-*me*PPy-GAC.

Figure 3 shows the scanning electron micrographs of PPy (a), *me*PPy-NPs (b), GAC (c) and P-*me*PPy-GAC (d). The micrograph of PPy displays the typical morphological features of irregular structures of agglomerated spherical-like particles, which is commonly observed for PPy obtained by chemical oxidation polymerization.[20] In contrast, the micrographs for *me*PPy-NPs display a predominance of smaller-sized, less densely packed aggregates of spherical-like shape particles, suggesting significant improvement in the physical properties of PPy obtained by microemulsion polymerization technique.

Meanwhile, the GAC particles micrographs display a dense structure of large, smooth, cracked faces and fissures with a slight presence of macropores. However, upon modification, the presence of evenly distributed spherical-like particles on the GAC surface are clearly visible from the P-*me*PPy-GAC micrographs, indicating the successful attachment of *me*PPy-NPs by the electrospraying technique.

Transmission electron micrographs of GAC, mePPy-NPs, and P-mePPy-GAC are shown in **Figures 4a–c**, respectively. The GAC micrographs show the presence of a highly disordered structure which corresponds to non-graphitized carbon materials. Meanwhile, the mePPy-NPs micrographs exhibit the presence of spherical particles with an average diameter of ≈94 nm, confirming the formation of PPy nanoparticles by microemulsion polymerization. Furthermore, the P-mePPy-GAC image shows a uniform dispersion of the mePPy-NPs adhering on the GAC surface, as notable by the dark portions of spherical particles.

Given that the P-*me*PPy-GAC nanocomposite is designed to be used as an adsorbent material, adhesive forces of nanoparticles onto the GAC substrate are critical so to ensure that *me*PPy NPs do not detach from the surface of GAC particles because of friction during storage or in a fixed bed column during the water treatment process. As a result, in our previous study,[14] we reported the presence of the *me*PPy NPs of the surface of the GAC and the extent of adhesive forces between the *me*PPy NPs and the GAC surface. AFM imaging was used to investigate the nanoscopic topography of the nanocomposite including its surface roughness, and the adhesion of the nanoparticle to the surface of the GAC. The roughness analysis revealed an effective deposit of *me*PPy NPs onto the GAC surface, with the highest peak recorded at 675 nm, suggesting two or three *me*PPy NPs layers of 200 nm average thickness coating on the GAC surface. In addition, the force spectroscopy analysis showed that the nanoparticles were successfully attached to one side of the GAC surface with a relatively strong adhesion force amounting to 10.8 nN on average.

3.2. Batch Adsorption

3.2.1. Effect of pH

Solution pH plays a significant role in adsorption processes as it governs the protonation or deprotonation of target compounds in the aqueous phase and the surface charge density of the adsorbent. Adsorption of Cr(VI) onto P-*me*PPy-GAC as a function of pH is demonstrated in **Figure 5**.

It appears that the removal of Cr(VI) decreases with increasing solution pH from 2 to 8. Specifically, the extent of Cr(VI) removal
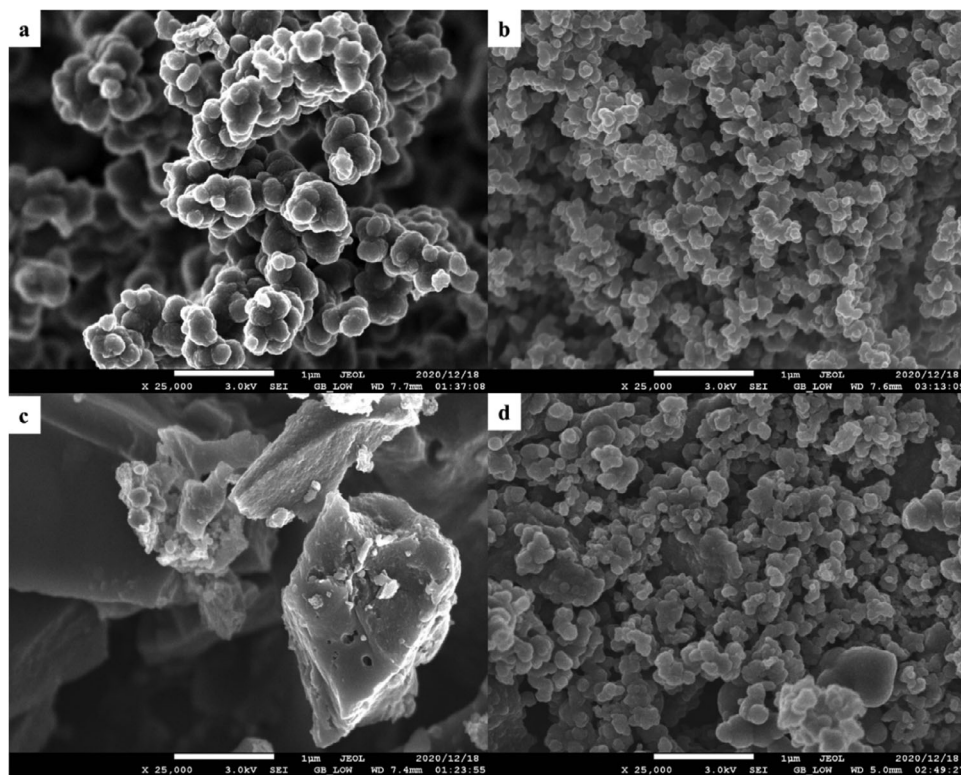
ADVANCED
SCIENCE NEWS

www.advancedsciencenews.com

{M} acro-
olecular
Materials and Engineering
Open Access

www.mame-journal.de

Figure 3. Scanning electron micrographs of a) PPy, b) mePPy-NPs, c) GAC and d) P-mePPy-GAC.
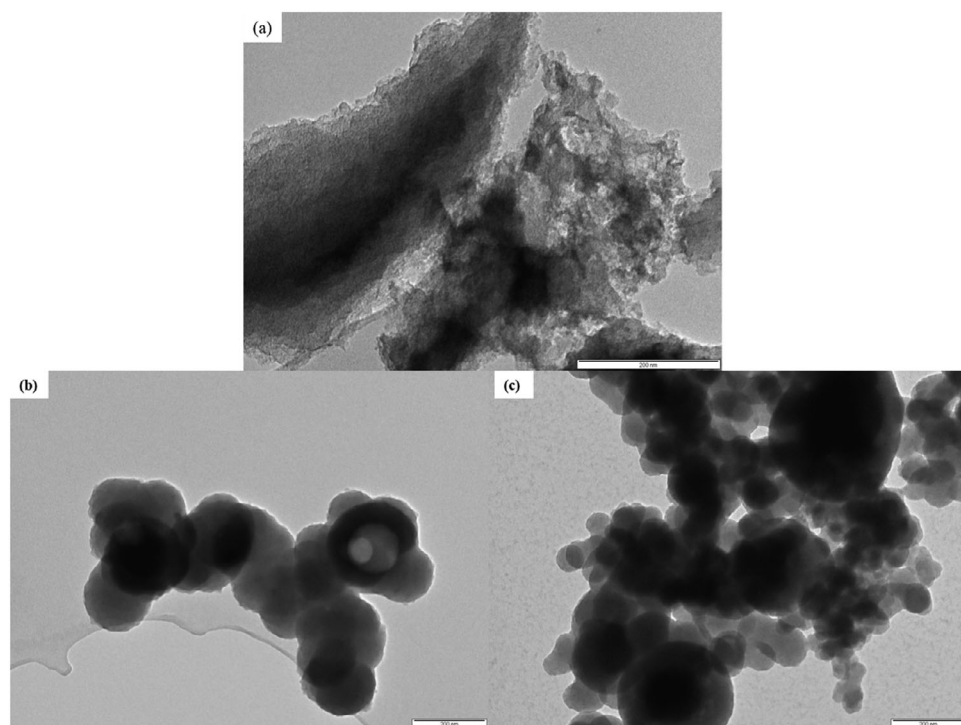
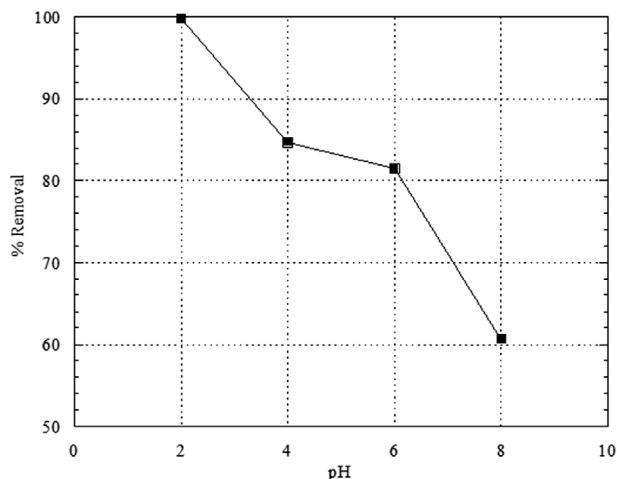**Figure 4.** Transmission electron micrographs of a) GAC, b) *me*PPy-NPs, and c) P-*me*PPy-GAC.

ADVANCED
SCIENCE NEWS
www.advancedsciencenews.com

[M]acro-
molecular
Materials and Engineering
Open Access

www.mame-journal.de

Figure 5. The effect of pH on Cr(VI) adsorption onto P-*me*PPy-GAC.

Figure 6. Adsorption kinetics of Cr(VI) onto PPy, GAC, (in situ)-PPy-GAC, and P-*me*PPy-GAC.

decreases from maximum of 99.99% to 60% with increase in pH from 2 to 8. This observation can be illustrated based on PZC, as the surface of the adsorbent likely to be positively charged at pH < PZC and negatively charged at pH > PZC. According to Figure 1, the PZC of the P-*me*PPy-GAC was found to be 7.5, indicating that at lower pH values, the adsorbent surface is highly protonated which favored binding of negatively charged Cr(VI) ions electrostatically. While in alkaline medium (pH > 7), the presence of large amount of hydroxyl ions (OH⁻) in the aqueous solution start competing with the Cr(VI) ions for the P-*me*PPy-GAC binding sites, resulting in meagre sorption of Cr(VI) ions.

3.2.2. Adsorption Kinetics

The adsorption kinetics of Cr(VI) onto PPy, GAC, (in-situ)-PPy-GAC, and P-*me*PPy-GAC were evaluated and data is shown in **Figure 6**. The plots of q_t versus t display similar adsorption profile of increasing Cr(VI) uptake with contact time, characterized by a rapid uptake in the first 15 min which slowed down to a plateau in ≈150 min toward equilibrium. The recorded amounts of Cr(VI) adsorbed from 0–150 min were 42.49, 55.91, 112.66, and 161.22 mg g⁻¹ for PPy, GAC, (in situ)-PPy-GAC and P-*me*PPy-GAC, respectively.

Based on the results, it is evident that the Cr(VI) removal performance of GAC was enhanced by more than threefold to its individual performance after electro-spraying with *me*PPy-NPs. While an exceptional improvement on the GAC performance by *me*PPy-NPs is realized, PPy alone shows a rather poor, although comparable performance to GAC for Cr(VI) removal as compared to its composite (in situ)-PPy-GAC. Moreover, the quantified amount of *me*PPy-NPs coated on GAC was <1% of the sorbent dosage used per batch and hence a significant reduction in the polymer requirement and cost.

In order to understand the adsorption kinetic mechanism of Cr(VI) and potential rate-controlling steps such as diffusion mass transport and chemical reaction processes, experimental data were analyzed using various kinetic models, including the Lagergren[21] and Ho[22] psued-first-order and pseudo second order models, respectively. The linearized forms of the pseudo-first-
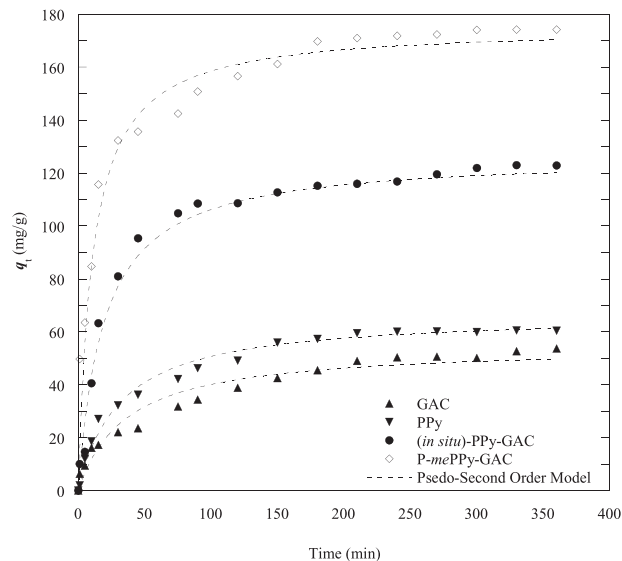
order, pseudo-second-order equations are given in Equations (4) and (5), respectively,

$$\ln\left(q_e - q_t\right) = -k_1\, t + \ln q_e \tag{4}$$

$$\frac{t}{q_t} = \frac{1}{k_2 q_e^2} + \frac{t}{q_e} \tag{5}$$

where k_1 (1/min) and k_2 (g/mg/min) are the pseudo-first order and pseudo-second order rate constants, respectively. The linearized plots of Equations (3) and (4) are shown in **Figures 7a,b**, respectively, and the values of q_e, rate constants and correlation coefficients determined from these plots are summarized in **Table 2**. Accordingly, based on the high correlation coefficients (R^2) of > 0.97 and the similarity between the calculated and experimental q_e values, the removal of Cr(VI) was best described by the pseudo-second order mechanism. Besides, the non-linear form of the pseudo-second order model plots in Figure 7, clearly shows better conformity with experimental data than the pseudo-first-order model.

Meanwhile, in order to gain insight into the mechanisms and rate controlling steps affecting the kinetics of adsorption, experimental data were analyzed using the Weber-Morris intra-particle diffusion model given by the relationship between time-dependent adsorption capacity q_t and $t^{1/2}$ in Equation (6),

$$q_t = k_p\, t^{\frac{1}{2}} + C \tag{6}$$

where k_p is the intra-particle diffusion rate constant (mg.g⁻¹min⁻¹/²) and C is the intercept (mg.g⁻¹) which provides information about the boundary layer thickness.[23] The model assumes that if the plot of q_t versus $t^{1/2}$ is linear and passes through the origin, the adsorption process is solely controlled by intraparticle diffusion; However, in certain occasions whereby the plot of q_t versus $t^{1/2}$ is multilinear, then two or more steps then govern the sorption process. The q_t versus $t^{1/2}$ plots

ADVANCED
SCIENCE NEWS
www.advancedsciencenews.com

[M] acro-
olecular
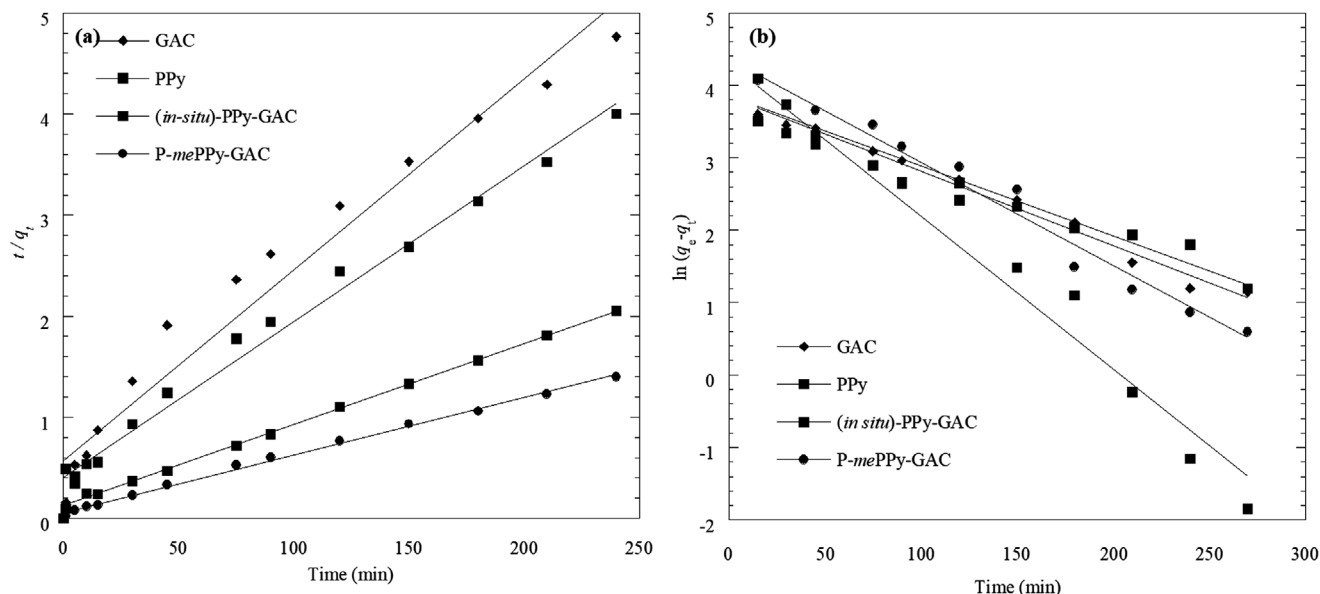Materials and Engineering
Open Access
www.mame-journal.de

Figure 7. Linearized a) pseudo-first order and b) pseudo-second order models for Cr(VI) sorption onto PPy, GAC, (in situ)-PPy-GAC, and P-*me*PPy-GAC.

obtained for Cr(VI) uptake onto GAC, PPy, (in situ)-PPy-GAC and P-mePPy-GAC are shown in **Figure 8**, and their corresponding calculated parameters (k_p and C) are summarised in **Table 3**.

According to Figure 8, the q_t versus $t^{1/2}$ plots exhibit multi-linear profiles, each with three distinct linear regions, suggesting that the adsorption process occurred in three stages. In the first linear segment of the plots, a sudden increase in the adsorption capacity takes place, indicating surface or film diffusion of Cr(VI) ions to the external surface of the adsorbent (boundary film diffusion). This is followed by the gradual adsorption stage in the second linear segment, where intra-particle or pore diffusion is dominant. The last segment indicates final equilibrium stage where intraparticle diffusion slows down due to the low Cr(VI) concentration left in the solution.[24,25] The calculated intraparticle diffusion rate constant k_p values, obtained from the slopes of the linear segments (Table 3), display a decreasing trend from stage 1 (1st linear segment) to stage 3 (2nd linear segment), suggesting that indeed surface diffusion proceeds faster than intraparticle diffusion.[8,26]

According to the intraparticle diffusion model, it is evident that sorption of Cr(VI) onto GAC, PPy, (in situ)-PPy-GAC and P-mePPy-GAC is a complex and multi-stage process. However, the process which governs the overall rate of adsorption process re-mains uncertain, and thus needs to be addressed. Consequently, the Boyd mathematical expression[27] was used to predict the actual rate-determining step in the sorption process. The Boyd model expression is represented by Equation (7),

$$F = 1 - \frac{6}{\pi^2} \sum_{m=1}^{\infty} \frac{1}{m^2} exp \left[\frac{-D_i \pi^2 m^2 t}{r^2} \right] \qquad (7)$$

or

$$F = 1 - \frac{6}{\pi^2} \sum_{m=1}^{\infty} \frac{1}{m^2} exp \left(-m^2 Bt \right) \qquad (8)$$
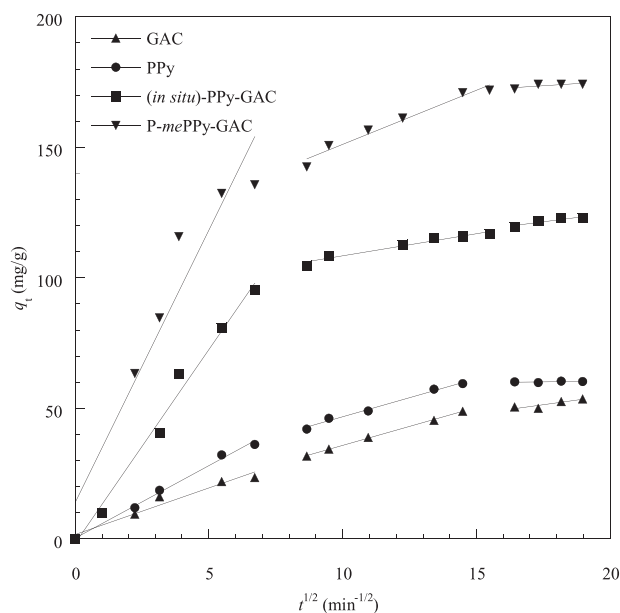

Figure 8. Intraparticle diffusion model plots for Cr(VI) sorption onto PPy, GAC, (in situ)-PPy-GAC, and P-*me*PPy-GAC.

Table 2. Summary of pseudo-first-order and pseudo-second-order kinetic data.

Adsorbents	Pseudo-second-order model			Pseudo-first-order model		
	q_e (mg/g)	k_2 (g/mg/min)	R^2	q_e (mg/g)	k_1 (L mi^{-1}n)	R^2
GAC	54.64	0.29×10^{-3}	0.996	46.46	0.011	0.995
PPy	66.67	0.46×10^{-3}	0.998	74.56	0.021	0.993
(in situ)-PPy-GAC	126.6	0.44×10^{-3}	0.999	47.27	0.012	0.996
P-*me*PPy-GAC	175.4	0.11×10^{-3}	0.996	77.94	0.012	0.969

ADVANCED
SCIENCE NEWS

www.advancedsciencenews.com

Macro-
molecular
Materials and Engineering
Open Access

www.mame-journal.de

Table 3. Intraparticle diffusion model parameters for PPy, GAC, (in-situ)-PPy-GAC, and P-*me*PPy-GAC.

| | Intraparticle diffusion model parameters/linear segments | | | | | | | | |
| | 1st Linear Segment | | | 2nd Linear segment | | | 3rd Linear segment | | |
Adsorbents	k_p	C	R^2	k_p	C	R^2	k_p	C	R^2
GAC	3.57	1.68	0.976	2.90	6.79	0.999	1.10	34.5	0.979
PPy	5.56	0.250	0.997	2.00	2.93	17.5	3.00	0.180	57.3
(in situ)-PPy-GAC	14.9	1.72	0.993	2.00	1.70	91.4	1.31	98.5	0.910
P-*me*PPy-GAC	20.9	13.9	0.961	4.15	109	0.984	0.670	162	0.818

where F is the fractional attainment of equilibrium at time t and is obtained by the expression:

$$F = \frac{q_t}{q_e} \tag{9}$$

where q_t (mg/g) and q_e (mg/g) are the time dependent and the maximum equilibrium Cr(VI) uptake, respectively, and

$$B = \frac{D_i \pi^2}{r^2} \tag{10}$$

where B is the time constant (min^{-1}), D_i is the effective diffusion coefficient of the metal ions in the sorbent phase (cm^2/min), r is the radius of the sorbent particle (cm), assumed to be spherical, and m is an integer that defines the infinite series solution. Bt is given by Equation (11),

$$Bt = -0.4977 - \ln(1 - F) \tag{11}$$

where the values of Bt calculated for each value of F, were plotted against time (t) to construct the Boyd's plots (Bt vs t). The theory behind the Boyd plots is that if plot is linear and passes through the origin, then particle diffusion considered to be the rate limiting step, however if the plot is linear but does not pass through the origin then external mass transfer governs the overall rate of the sorption removal.[23,28]

Figure 9 illustrates the Boyd plots for Cr(VI) adsorption on GAC, PPy, (in situ)-PPy-GAC and P-*me*PPy-GAC, and **Table 4** list the obtained model parameters from the Boyd plots. As displayed in Figure 9, it can be noted that all the Boyd plots exhibit a linear relationship, and do not pass through the origin. Accordingly, these indicate that the adsorption of Cr(VI) onto GAC, PPy, (in situ)-PPy-GAC and P-*me*PPy-GAC was governed by film diffusion or chemical reaction.[23,28,29]

3.2.3. Adsorption Equilibrium Isotherms

The equilibrium isotherm data of Cr(VI) adsorption onto P-*me*PPy-GAC were generated over a wide concertation range (100–700 mg L^{-1}) at varying temperatures from 298K–318K, and data is shown in **Figure 10**. Accordingly, the plots of q_e versus C_e display an increase in Cr(VI) uptake with increasing temperature and equilibrium concentration. The increase in Cr(VI) uptake with temperature suggests that the Cr(VI) sorption process onto
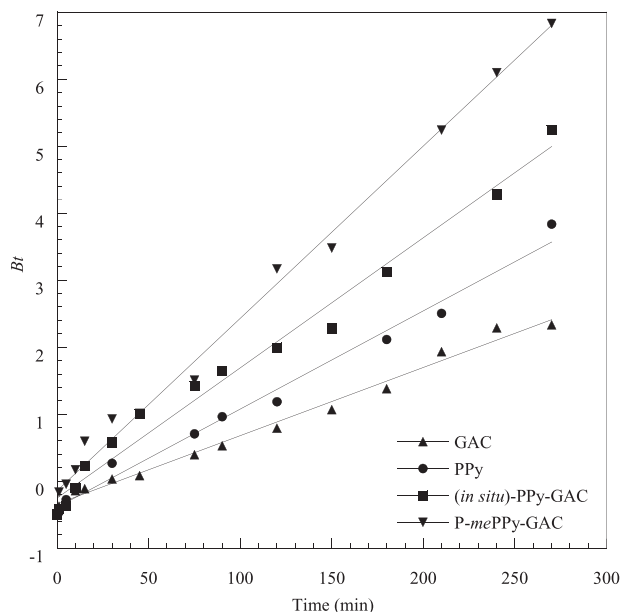
Figure 9. Boyd plots for Cr(VI) sorption onto PPy, GAC, (in situ)-PPy-GAC, and P-*me*PPy-GAC.

Table 4. Boyd kinetic model parameters for Cr(VI) sorption onto PPy, GAC, (in-situ)-PPy-GAC, and P-*me*PPy-GAC.

| | Boyd Plot parameters | |
Adsorbents	Intercept	R^2
GAC	−0.341	0.995
PPy	−0.394	0.994
(in-situ)-PPy-GAC	−0.249	0.992
P-*me*PPy-GAC	0.138	0.997
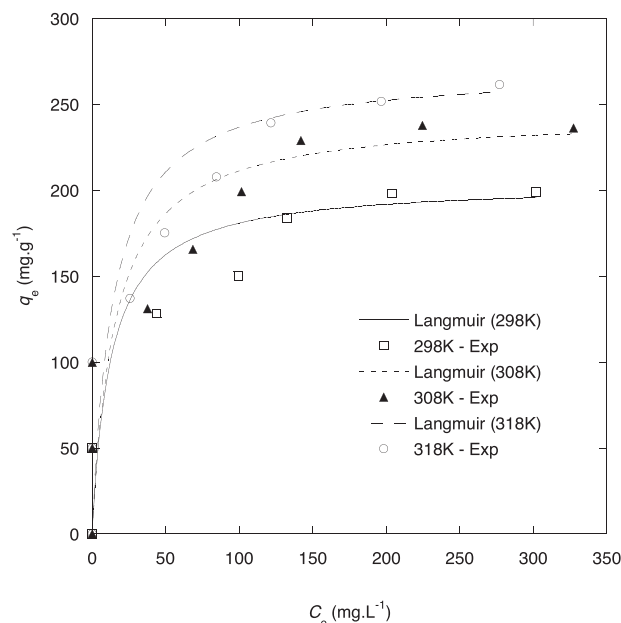
Figure 10. Sorption isotherms of Cr(VI) sorption onto P-*me*PPy-GAC at temperatures 298, 308 and 318 K.

**ADVANCED
SCIENCE NEWS**

www.advancedsciencenews.com

{M}acro-
molecular
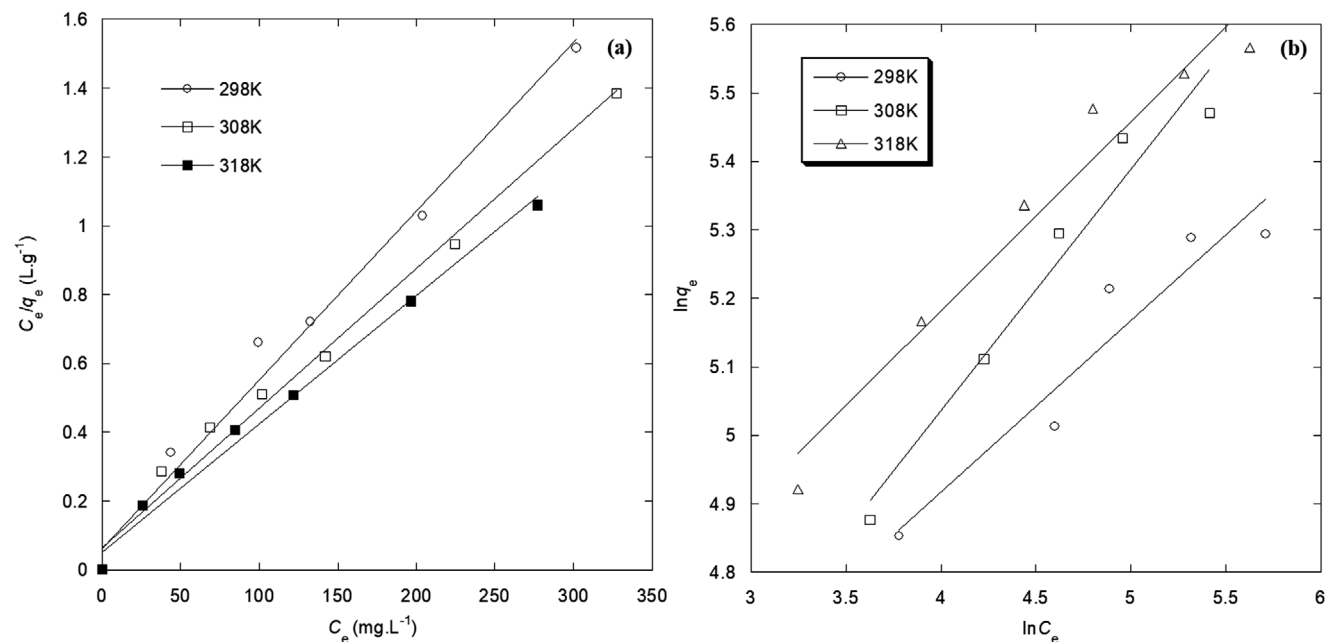Materials and Engineering
Open Access

www.mame-journal.de

Figure 11. Linearized a) Langmuir and b) Freundlich isotherms for Cr(VI) sorption onto P-*me*PPy-GAC.

P-*me*PPy-GAC was endothermic. Increasing temperature affects sorption process by increasing the thermal energy of adsorbed species, which may have increased the mobility and the driving force of the Cr(VI) ions toward the active site of P-*me*PPy-GAC leading to higher uptake.[30,31] Furthermore, the concentration gradient of adsorbed species is known to act as a driving force during adsorption processes, which is generated at elevated concentrations to overcome all mass transfer resistance between the aqueous and solid phases and as a result, may be attributed to the increased Cr(VI) uptake with concentration.[8]

Meanwhile, to examine the relationship between the adsorbed Cr(VI) amounts (q_e) and concentration (C_e) in the liquid phase, mathematical sorption isotherm models including the Langmuir and Freundlich models, were employed to analyze experimental data. The Langmuir isotherm model assumes monolayer sorption on the adsorbent surface with identical sorption sites expressed, while the Freundlich model assumes adsorption on a heterogeneous surface.[32] The linearized form of the Langmuir isotherm model is given in Equation (12),

$$\frac{C_e}{q_e} = \frac{1}{q_{max}b} + \frac{C_e}{q_{max}} \tag{12}$$

where q_{max} (mg.g^{-1}) is the maximum amount of Cr(VI) ions per unit mass of adsorbent to form a complete monolayer on the adsorbent surface and b (L.mg^{-1}) is the binding energy constant. Furthermore, the dimensionless separation factor, R_L, which is an essential characteristic of the Langmuir model for defining the favorability of an adsorption process, was used and is given in Equation (13),

$$R_L = \frac{1}{(1 + bC_o)} \tag{13}$$

whereby if the average of the R_L values for each of the different initial concentration used is between 0 and 1 indicates a favorable adsorption process. Furthermore, the Freundlich isotherm model is expressed in Equation (14),

$$\ln q_e = \ln K_F + \frac{1}{n} \ln C_e \tag{14}$$

where K_F (mg.g^{-1}) and $1/n$ constants are related to the adsorption capacity and intensity of adsorption, respectively. The plots of linearized Langmuir and Freundlich isotherms are shown in **Figures** 11a,b. and their respective parameters calculated from the slopes and intercepts of linear graphs are summarized in **Table 5**.

Considering the higher correlation coefficient achieved from the Langmuir model ($R^2 > 0.98$) as compared to the Freundlich model ($R^2 < 0.96$), as well as the similarities between the calculated (q_o, K_F) and experimental (q_e) sorption capacities, it is clear that the sorption process of Cr(VI) onto P-*me*PPy-GAC is well described by the Langmuir isotherm model. The calculated Langmuir maximum sorption capacities of P-*me*PPy-GAC show an increase in Cr(VI) uptake from 204.08 to 270.27 mg g^{-1} as the temperature increased for recorded as calculated as show an increased from 298 to 318 K. Furthermore, the non-linear forms

Table 5. Langmuir and Freundlich isotherm parameters for Cr(VI) sorption onto P-*me*PPy-GAC.

T(K)	Langmuir constants				Freundlich constants		
	q_{max} (mg.g^{-1})	b (L/mg)	R^2	R_L	K_F	$1/n$	R^2
298	204.08	0.078	0.986	0.044	50.04	0.25	0.913
308	243.90	0.065	0.987	0.048	37.57	0.35	0.958
318	270.27	0.071	0.989	0.045	58.87	0.28	0.955

www.advancedsciencenews.com

[M] macro-molecular
Materials and Engineering
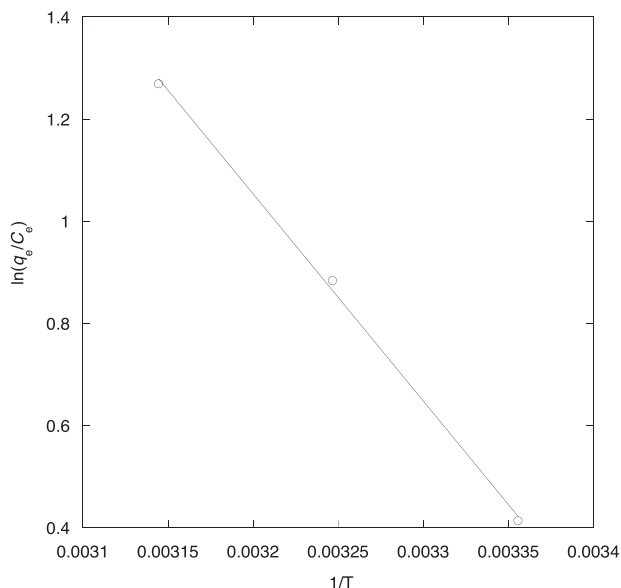Open Access
www.mame-journal.de

Figure 12. Van't Hoff plots for Cr(VI) sorption onto P-*me*PPy-GAC.

of the Langmuir plots in Figure 10 display a good fit with experimental data for all temperatures, thus validating the model's conformity toward the process description. The average R_L values at different temperatures were found to be in a range 0–1, which is consistent with a favorable adsorption process.

Thermodynamic parameters such as change in Gibbs free energy ($\Delta G°$), enthalpy ($\Delta H°$) and entropy ($\Delta S°$) were evaluated to assess the spontaneity of the Cr(VI) sorption process onto P-*me*PPy-GAC using Equations (15) and (16),

$$\ln\left(\frac{q_e}{C_e}\right) = \frac{\Delta S°}{R} + \frac{-\Delta H°}{RT} \tag{15}$$

$$\Delta G° = -RT\ln\left(\frac{q_e}{C_e}\right) \tag{16}$$

where R (J.mol^{-1}.K^{-1}) is the gas constant and T (K) is the temperature. The values of $\Delta H°$ and $\Delta S°$ were obtained from the slope and intercept of the linear Van't Hoff plots of $\ln(q_e/C_e)$ versus $1/T$ displayed in **Figure 12** are summarized in **Table 6**. The decrease in free energy with an increasing temperature indicates that adsorption of Cr(VI) onto P-*me*PPy-GAC was spontaneous in nature. The positive value of $\Delta S°$ (116.69 J.mol^{-1}.K^{-1}) suggest an increase in disorder at the solid-liquid interface, while the positive $\Delta H°$ (33.73 kJ mol^{-1}) is consistent with the endothermic nature of the sorption process.

Table 6. Thermodynamic parameters for Cr(VI) adsorption onto P-*me*PPy-GAC.

T(K)	$\Delta S°$	$\Delta H°$	$\Delta G°$
	116.60	33.72	
298			−1.02
308			−2.19
318			−3.14

3.2.4. Fixed-Bed Column Adsorption Dynamics of the P-*me*PPy-GAC

Continuous fixed-bed adsorption studies were carried out to investigate the breakthrough performance of P-*me*PPy-GAC for Cr(VI) removal in comparison with the non-modified pristine GAC. The initial Cr(VI) concentration, bed mass, bed height, and flow rate were fixed at 10 mg L^{-1}, 5 g, 4 cm and 3 mL min^{-1}, respectively. The performance of the packed bed column is expressed using the theory of breakthrough curves as they provide information about the breakthrough point, which is the point in time where the effluent concentration exceeds the maximum allowable discharge concentration regulated for a given contaminant. The breakthrough curves can be obtained by plotting the dimensionless concentration C_t/C_o versus time or volume of the effluent. In this study, the U.S. Environmental Protection Agency (US-EPA) regulatory surface water discharge limit of 0.1 mg L^{-1} Cr (VI) was used to evaluate the column performance indicators including the empty bed contact time (EBCT, min), number of bed volumes (NBV), breakthrough capacity (q_b, mg.g^{-1}), equilibrium capacity (qe, mg.g^{-1}) and adsorbent exhaustion rate (AER, g.l^{-1}) given in Equations (17) to (21), respectively,

$$ECBT = \frac{z}{(QA_c)} \tag{17}$$

$$NBV = \frac{V_{Bt}}{V_b} \tag{18}$$

$$q_b = \frac{Q}{1000}\int_0^{t_b}(C_o - C_b)\,dt \tag{19}$$

$$q_e = \frac{Q}{1000}\int_0^{t_e}(C_o - C_t)\,dt \tag{20}$$

$$AER = \frac{m}{V_t} \tag{21}$$

where, z (cm) is bed height, Q (mL.min^{-1}) is flow rate, A_C (cm^2) is column cross section area, V_{Bt} (L) is the volume treated at
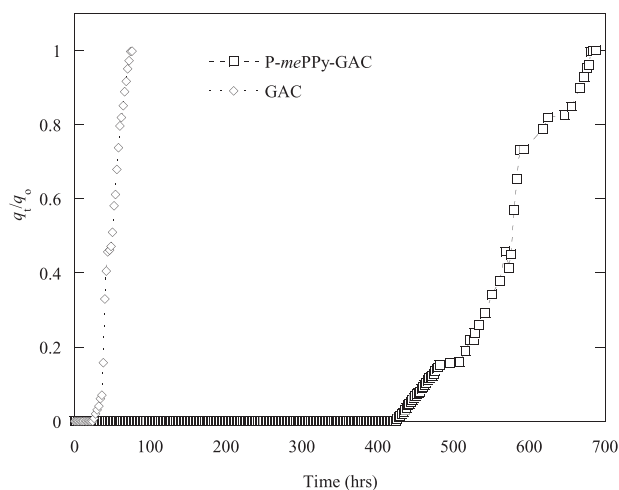

Figure 13. Performance comparison breakthrough curves of P-*me*PPy-GAC and GAC for Cr(VI) sorption.

Table 7. Summary of breakthrough pertinent results for Cr(VI) sorption onto P-*me*PPy-GAC and GAC.

Parameters	P-*em*Ppy-GAC$^{T\text{-}charged}$	GAC
t_b (min)	25 680	780
t_e (min)	41 280	6900
V_b (L)	77.04	2.34
NBV	9579	291
q_b (mg.g^{-1})	1.5408	0.0468
V_t (L)	123.84	20.7
q_e	247.68	41.4
AER (g.L^{-1})	0.04	0.24

breakthrough, V_b (L) is the bed volume, C_b and C_t are the solute concentrations at breakthrough and time, t, while t_b (min) and V_t (L) are breakthrough time and the total treated volume, respectively.[33] The breakthrough performance of P-*me*PPy-GAC for Cr(VI) was compared to that of GAC and data are shown in **Figure 13**.

The breakthrough plots display higher Cr(VI) removal performance with P-*me*PPy-GAC as compared to GAC. Specifically, the breakthrough points recorded for Cr(VI) sorption onto P-*me*PPy-GAC and GAC were 428 h and 13 h, respectively. This exceptional P-*me*PPy-GAC performance indicates that the GAC sorption performance was significantly improved by modification with PPy.

From the pertinent performance data summarized in **Table 7**, the treated volumes of Cr(VI) effluent at breakthrough were recorded as 77.04 L and 2.34 L for P-*me*PPy-GAC and GAC, respectively. Higher NBVs and lower AER values were recorded for P-*me*PPy-GAC. The lower AER values indicate that the exhaustion rate of P-*me*PPy-GAC during Cr(VI) sorption was slower than that of GAC. Furthermore, the maximum equilibrium Cr(VI) uptakes of 247.68 mg g^{-1} and 41.40 mg g^{-1} were recorded for P-*me*PPy-GAC and GAC, respectively.

3.2.5. Cr(VI) Adsorption from Industrial Wastewater

While the P-*me*PPy-GAC showed an impressive performance for the removal of Cr(VI) from aqueous solutions in both batch and continuous fixed-bed adsorption modes, it was necessary to further evaluate its performance in relevant wastewater samples. Consequently, wastewater sample containing 68 μg L^{-1} of Cr(VI) was obtained from a ferrochrome industry (South Africa) whereby the P-*me*PPy-GAC was evaluated for Cr(VI) removal in terms of adsorption reaction kinetics studies. In this study, 1 L of the industrial sample was contacted with a fixed amount of the P-*me*PPy-GAC (1 g) in a glass beaker as a reactor model, and stirred at 200 rpm using an overhead stirrer. Subsequently, 10 mL samples were withdrawn at predetermined time interval and analyzed for residual Cr(VI) concentrations. Displayed in **Figure 14**, the kinetic data show a rapid uptake of Cr(VI) onto P-*me*PPy-GAC in the first 30 s, which interestingly also characterizes the equilibrium point. Specifically, data show that the P-*me*PPy-GAC was able to remove >80% of the Cr(VI) from the wastewater, leaving only <14 μm L^{-1} which is below allowable Cr(VI) discharge limit of 50 μg L^{-1}. The residual concentration of Cr in the treated medium was not accurately determined owing to the relatively high detection limit of the UV spectrophotometry used for evaluation. We can assume with a high degree of confidence that Cr was removed at 99% and more.

3.2.6. Desorption and Regeneration

In an attempt to re-activate the spent P-*em*Ppy-GACT-charged nanocomposite laden with Cr (VI), a study was performed aiming to establish the appropriate system of solvents, which are able to efficiently regenerate and restore the binding sites of the nanocomposite by desorbing Cr (VI) followed by a subsequent re-doping of the adsorbent surface with a specific counter-ion. At this effect, five legs of the experimental design with various combinations of solvents were suggested as depicted in **Table 8**.
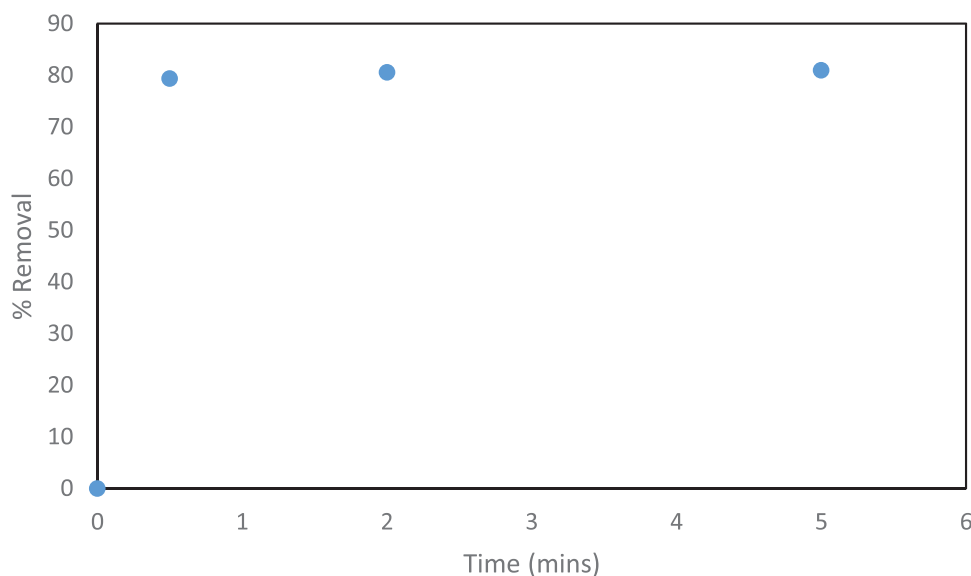

Figure 14. Sorption kinetics of Cr(VI) sorption from industrial wastewater onto P-*me*PPy-GAC.

**ADVANCED
SCIENCE NEWS**

www.advancedsciencenews.com

**M⸺acro-
⸺olecular
Materials and Engineering**

www.mame-journal.de

Table 8. Adsorption and desorption cycles of Cr(VI).

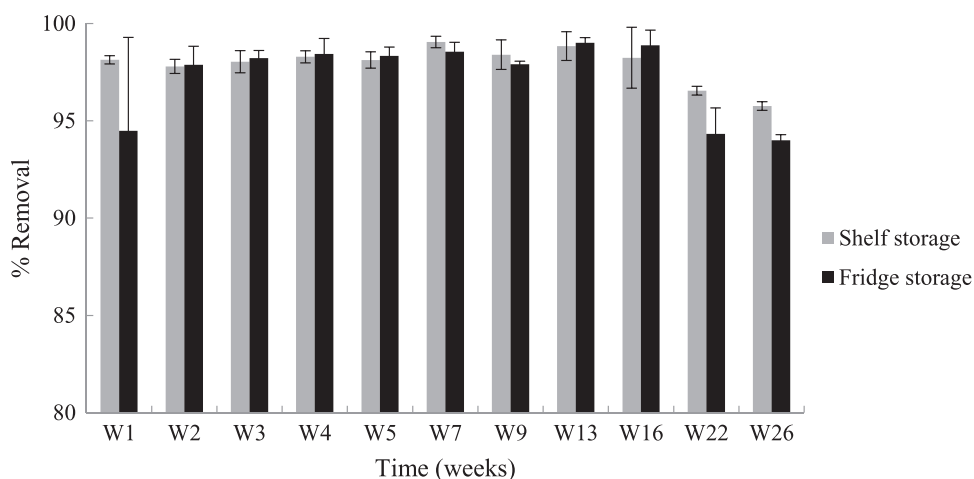|	NaOH [M]	HCl [M]	CH$_3$OOH	EtOH [%v/v]	Temp. [°C]	% Removal 1st cycle	% Desorbed	% Removal 2nd cycle
Plan A	0.05	0.05	–	–		99.9	12.09	90.90
Plan B	0.05	–	0.05	–		99.8	10.53	88.43
Plan C	–	–	–	10	60	99.9	3.541	93.58
Plan D	–	–	–	–	–	98.73	–	90.45
Plan E	0.05	–	–	10	60	99.8	10.9	96.74

Figure 15. Removal efficiencies of P-mePPy-GAC at two different storage conditions.

It should be noted that the removal efficiency of Cr (VI) in the second cycle for all schemes were slightly reduced. A combination of alkali as desorbent and ethanol as re-activating agent, resulted in a high efficiency in the second cycle of chrome removal; However, Plan B resulted in a lower efficiency owing to the use of acetic acid as a new dopant. Acetic acid has a lower degree of mobility as compared to initial chloride anions, thus low kinetic of ion exchange with chromate anions.

3.2.7. Ageing Stability Study of P-mePPy-GAC

For a practical use of PPy-based materials, durability and storage stability are important aspects in any application. It is worth noting that the combination oxygen (air) and moisture is reported as the major source of decay of PPy properties owing to the positioning of its double chain being susceptible to oxidative reactions. A prolonged exposure to oxygen might equally result in a decrease of its adsorptive ion exchange properties. It appears therefore crucial to monitor the structural alterations of PPy-based materials as well as their adsorptive performance. Accordingly, the stability and shelf life assessment of the P-mePPy-GAC for Cr(VI) adsorption performance was evaluated over a period of 6 months under different temperature conditions. In a typical experiment, two batches of 12 grams each were stored in air tied containers separately; one was stored on the benchtop at ambient conditions while the other one was stored in a fridge at 8 °C. Performance data for Cr(VI) sorption were generated in a batch mode under the following conditions: 200 mg L^{-1} Cr(VI) concentration, solu-

tion pH 2, and 0.1 g of P-mePP-GAC. All tests were carried out in triplicates for 24 h.

The aliquot sample at a predetermined time was tested for Cr (VI) removal performance. Surprisingly, both samples maintained their adsorptive surface properties over a period of more than 20 weeks. However, a slight decrease in efficiency was noticed from week 22, but the removal capacity of Cr (VI) remained appreciable as shown in **Figure 15**.

4. Conclusion

This study focused on the development of a PPy coated GAC nanocomposite adsorbent material (P-mePPy-GAC) for the removal of Cr(VI) from aqueous solutions. In this instant, a successful technique that was devised to produce PPy nanoparticles (≈200 nm) with a narrow size distribution by employing a soft template technique has been reported. These nanoparticles were electrostatically deposited on one face of GAC particles by electrospraying a suspension of the former onto the latter, to which transient electrostatic charges were imparted by means of tribocharging on a paper substrate. The resulting P-mePPy-GAC nanocomposite structure was characterized by different techniques, including BET, FTIR, SEM, and TEM. The adsorption performance of the P-mePPy-GAC for Cr(VI) removal from aqueous solutions in a batch and continuous fixed-bed column modes of adsorption. Under a wide range of experimental conditions, the P-mePPy-GAC displayed an exceptional performance for Cr(VI) removal from aqueous solution, with a recorded fourfold Cr(VI) uptake capacity increase as compared to pristine GAC.

ADVANCED
SCIENCE NEWS

www.advancedsciencenews.com

Macro-
molecular
Materials and Engineering
Open Access

www.mame-journal.de

Moreover, the uptake of Cr(VI) from aqueous solutions increased with an increase in temperature, initial Cr(VI) concentration and a decrease in solution pH.

The Cr(VI) sorption kinetic data were well described by the pseudo-second-order model, whereas the Weber-Morris intra-particle diffusion model and Boyd kinetic model proved the main controlling step for the adsorption process was diffusion through the boundary layer. The sorption equilibrium data were well described by the Langmuir isotherm model, with maximum Cr(VI) sorption capacities of 204.08, 243.9, and 270.27 mg g^{-1} for 298, 308, and 318 K, respectively. Moreover, the adsorption process was spontaneous with a positive enthalpy (33.7 kJ mol^{-1}) describing an endothermic reaction. When the latter was tested for the continuous removal of Cr(VI) in a fixed-bed adsorption column, a breakthrough time (t_b) of 428 h was achieved for P-*me*PPy-GAC as compared to 13 h for pristine GAC, and the subsequent volume of treated water at breakthrough (V_b) were 77 L and 2.3 L for P-*me*PPy-GAC and GAC, respectively.

Supporting Information

Supporting Information is available from the Wiley Online Library or from the author.

Acknowledgements

Conflict of Interest

The authors declare no conflict of interest.

Data Availability Statement

The data that support the findings of this study are available from the corresponding author upon reasonable request.

Keywords

[1] Blacksmith Institute's World's Worst Pollution Problems Report **2010**, www.worstpolluted.org (accessed: March 2023).
[2] T. S. Anirudhan, S. Jalajamony, P. S. Suchithra, *Colloids Surf., A* **2009**, *335*, 107.
[3] S. P. Dubey, K. Gopal, *J. Hazard. Mater.* **2007**, *145*, 465.
[4] F. Fu, Q. Wang, *J. Environ. Manage.* **2011**, *92*, 407.
[5] G. Crini, E. Lichtfouse, *Environ. Chem. Lett.* **2019**, *17*, 145.
[6] V. K. Gupta, I. Ali, T. A. Saleh, A. Nayaka, S. Agarwal, *RSC Adv.* **2012**, *2*, 6380.
[7] A. A. Alghamdi, A. Al-Odayni, W. S. Saeed, A. Al-Kahtani, F. A. Alharthi, T. Aouak, *Materials* **2019**, *12*, 2020.
[8] K. Z. Setshedi, M. Bhaumik, S. Songwane, M. S. Onyongo, A. Maity, *Chem. Eng. J.* **2013**, *222*, 186.
[9] R. Hao, Z. Ma, Z. Zeng, Y. Mao, B. Yuan, L. Wang, *Environ. Sci. Technol.* **2022**, *56*, 6, 3689.
[10] R. Karthik, S. Meenakshi, *Desalination and Water treatment* **2015**, *56*, 1587.
[11] J. Guo, L. Wang, Y. Tu, H. Muhammad, X. Fan, G. Cao, M. Laipan, *J. Environ. Chem. Eng.* **2021**, *9*, 106631.
[12] F. Wurm, A. F. M. Kilbinger, *Angew. Chem., Int. Ed.* **2009**, *48*, 8412.
[13] A. Perro, S. Reculusa, S. Ravaine, E. Bourgeat-Lamic, E. Duguet, *J. Mater. Chem.* **2005**, *15*, 3745.
[14] M. L. Kalombo, A. Adeniyi, N. Nomadolo, K. Setshedi, M. J. Madito, N. Manyala, R. K. Mbaya, *J. Taiwan Inst. Chem. Eng.* **2021**, *129*, 264.
[15] P. Melariri, L. Kalombo, P. Nkuna, A. Dube, R. Hayeshi, B. Ogutu, L. Gibhard, C. Dekock, P. Smith, L. Wiesner, H. Swai, *Int. J. Nanomed.* **2015**, *10*, 1493.
[16] T. L. A. Burgo, C. A. Silva, L. B. S. Balestrin, F. Galembeck, *Sci. Rep.* **2013**, *3*, 2384.
[17] J. Lowell, A. C. Rose-Innes, *Adv. Phys.* **1980**, *29*, 947.
[18] J. Wen, Y. Tian, Z. Mei, W. Wub, Y. Tian, *RSC Adv.* **2017**, *7*, 53219.
[19] F. Zhang, D. S. Wang, F. Yang, T. Y. Li, H. Y. Li, J. G. Cui, *Adv. Mat. Sci. Eng.* **2021**, *2021*, 1.
[20] S. Shrikrushna, J. A. K. Milind V Kulkarni, *J. Nanomed. Nanotechnol.* **2015**, *6*, 3.
[21] S. Lagergren, *Kungliga Svenska Vetenskapsakademiens Handlingar* **1898**, *24*, 1.
[22] Y. S. Ho, G. Mckay, D. A. J. Wase, C. F. Foster, *Adsorpt. Sci. Technol.* **2000**, *18*, 639.
[23] A. C. A. de Lima, R. F. Nascimento, F. F. de Sousa, M. Josue Filho, A. C. Oliveira, *Chem. Eng. J.* **2012**, *185*, 274.
[24] N. F. Al-Harby, E. F. Albahly, N. A. Mohamed, *Polymers* **2021**, *13*, 4446.
[25] Li, W., Sun, L., Xia, Z. U., X. Sun, Z. Wang, Y. Wang, X. Deng, *Molecules* **2022**, *27*, 7980.
[26] L. Mdlalose, M. Balogun, K. Setshedi, M. Tukulula, L. Chimuka, A. Chetty, *Appl. Clay Sci.* **2017**, *139*, 72.
[27] G. E. Boyd, A. W. Adamson Jr., L. S. Myers, *J. Am. Chem. Soc.* **1947**, *69*, 2836.
[28] S. Banerjee, G. C. Sharma, M. C. Chattopadhyaya, Y. C. Sharma, *J. Environ. Chem. Eng.* **2014**, *2*, 1870.
[29] P. Sharma, M. R. Das, *J. Chem. Eng. Data* **2013**, *58*, 151.
[30] Z. A. AL-Othman, R. Ali, M. Naushad, *Chem. Eng. J.* **2012**, *184*, 238.
[31] T. Karthikeyan, S. Rajgopal, L. R. Miranda, *J. Hazard. Mater.* **2005**, *124*, 192.
[32] H. Deng, L. Yang, G. Tao, J. Dai, *J. Hazard. Mater.* **2009**, *166*, 1514.
[33] E. Malkoc, Y. Nuhoglu, *Chem. Eng. Sci.* **2006**, *61*, 4363.